21 April 2026

Sodium expulsion from sodium closo-hydroborates under electron beam induced bias

Thomas S. Marchese[1,2], James N. Burrow[1,2], Nestor J. Zaluzec[1,3], Shuang Bai[1,2], Yuanlong Bill Zheng[1,4], Marta Vicencio[5], Venkata Surya Chaitanya Kolluru[2,6], Yu Chen[2,7,8], Maria K. Y. Chan[2,4], Minghao Zhang[1,2], Mary C. Scott[8,2,7], Y. Shirley Meng[1,2,5]

1. Pritzker School of Molecular Engineering University of Chicago
2. Energy Storage Research Alliance Argonne National Laboratory
3. Faculty of Engineering, Computing and Science Western Sydney University
4. Center for Nanoscale Materials Argonne National Laboratory
5. Department of Nano Engineering University of California San Diego
6. Department of Materials Science and Engineering Ohio State University
7. National Center for Electron Microscopy Molecular Foundry, Lawrence Berkeley National Laboratory
8. Department of Materials Science and Engineering University of California at Berkeley

Abstract

Electron microscopy (EM) invites the opportunity to locally characterize the properties of solid-state electrolytes important for choreographing ion motion within next-generation solid-state batteries. Through the combination of inert gas transfer, cryogenic, time-resolved low-dose analytical electron microscopy, we observe that mixed-anion sodium closo-hydroborate, Na2(B10H10)0.5(B12H12)0.5 (NBH), solid electrolyte suffers from electrostatic charging damage under bias of both transmission electron microscopes (TEM) and scanning electron microscopes (SEM). During the process of beam damage, crystalline ordering of NBH is lost, while particle morphology remains unchanged. In regions exposed to electron beams at a dose rate of 1-8 e- Å-2 s-1, spectroscopy confirms vastly reduced sodium signal or even absent from irradiated NBH at total doses less than 80 e- Å-2. Simultaneously, we detect the growth of sodium metal crystals on the unirradiated faces of NBH particles. An SEM experimental study revealed the maximum damage rate occurs at 2 keV with increasing energy prolonging the time before sodium extrudes. This work also highlights that cryogenic conditions, while highly effective in mitigating certain types of inelastic beam damage, are not the panacea for eluding beam sensitivity. Rather, comprehensive awareness of the underlying

physics in competing damage mechanisms is paramount in condition selection for battery interface characterization.

Sodium expulsion from sodium *closo*-hydroborates under electron beam induced bias

Running head: Sodium expulsion from sodium *closo*-hydroborates

Thomas S. Marchese[1,2], James N. Burrow[1,2], Nestor J. Zaluzec[1,3], Shuang Bai[1,2], Yuanlong Bill Zheng[1,4], Marta Vicencio[5], Venkata Surya Chaitanya Kolluru[2,6], Yu Chen[2,7,8], Maria K. Y. Chan[2,4], Minghao Zhang[1,2], Mary C. Scott[2,7,8*], Y. Shirley Meng[1,2,5*]

[1]Pritzker School of Molecular Engineering, University of Chicago, Chicago, IL, USA

[2]Energy Storage Research Alliance, Argonne National Laboratory, Lemont, IL, USA

[3]Western Sydney University, Faculty of Engineering, Computing and Science, NSW, Australia.

[4]Center for Nanoscale Materials, Argonne National Laboratory, Lemont, IL, USA

[5]Department of Nano Engineering, University of California San Diego, La Jolla, CA, USA

[6]Department of Materials Science and Engineering, The Ohio State University, Columbus, OH, USA

[7]National Center for Electron Microscopy, Molecular Foundry, Lawrence Berkeley National Laboratory, Berkeley, CA, USA

[8]Department of Materials Science and Engineering, University of California at Berkeley, Berkeley, CA 94720, USA

*Co-corresponding Authors

Conflicts of Interest: The authors declare that they have no competing interests.

Abstract

Electron microscopy (EM) invites the opportunity to locally characterize the properties of solid-state electrolytes important for choreographing ion motion within next-generation solid-state batteries. Through the combination of inert gas transfer, cryogenic, time-resolved low-dose analytical electron microscopy, we observe that mixed-anion sodium *closo*-hydroborate, $Na_2(B_{10}H_{10})_{0.5}(B_{12}H_{12})_{0.5}$ (NBH), solid electrolyte suffers from electrostatic charging damage under bias of both transmission electron microscopes (TEM) and scanning electron microscopes (SEM). During the process of beam damage, crystalline ordering of NBH is lost, while particle morphology remains unchanged. In regions exposed to electron beams at a dose rate of 1-8 $e^- Å^{-2} s^{-1}$, spectroscopy confirms vastly reduced sodium signal or even absent from irradiated NBH at total doses less than 80 $e^- Å^{-2}$. Simultaneously, we detect the growth of sodium metal crystals on the unirradiated faces of NBH particles. An SEM experimental study revealed the maximum damage rate occurs at 2 keV with increasing energy prolonging the time before sodium extrudes. This work also highlights that cryogenic conditions, while highly effective in mitigating certain types of inelastic beam damage, are not the panacea for eluding beam sensitivity. Rather, comprehensive awareness of the underlying physics in competing damage mechanisms is paramount in condition selection for battery interface characterization.

Introduction

Investigating interfacial mechanisms that govern solid-state batteries on the micro and nanoscale has the potential to inform future battery design (Zachman et al, 2018); (Boebinger et al, 2020); (Cheng et al 2022); (Banerjee et al, 2020). Sodium *closo*-hydroborates, a class of sodium solid-state electrolytes (SSE), have demonstrated state-of-the-art thermodynamic stability with sodium metal anodes (Deysher et al, 2022); (Deysher et al, 2024). Significant interest in the sodium all-solid-state battery field has focused on the mixed anion $Na_2(B_{10}H_{10})_{0.5}(B_{12}H_{12})_{0.5}$ composition (NBH), which crystallizes at room temperature in a face-centered cubic phase (typically exhibited by $Na_2(B_{10}H_{10})$ at high temperature) (Duchêne et al, 2017). This close-packed phase of NBH exhibits a high ionic conductivity of 1.7 mS cm^{-1} and a low electronic conductivity of $1.5x10^{-6}$ mS cm^{-1} at room temperature (Duchêne et al, 2017, 2019); (Yoshida et al, 2017). The remarkable stability toward reduction of NBH and associated lack of an apparent solid electrolyte interphase has enabled desirable anode-free solid-state battery configurations (Deysher et al, 2022); (Deysher et al, 2024). A fundamental understanding of sodium ion transport across the interface between NBH and sodium metal has yet to be achieved. As such, the desire for high-resolution imaging and characterization of the bulk structure and solid-solid interfaces of NBH solid electrolytes motivates the careful application of analytical transmission electron microscopy (EM). However, high-resolution imaging of alkali metals and SSE pose serious challenges due to the low melting points and high reactivity (Wang et al, 2017); (Zachman et al, 2018); (Bai et al, 2026). To this end, the field has adopted cryogenic transfer EM and imaging for studies of these materials (Han et al, 2021); (Li et al, 2021). Even with cryogenic EM, this work shows it is critical to monitor dose expenditure for beam damage when studying sensitive materials.

Modern electron microscopes encompass detectors that capture both the spatial and spectroscopic characteristics of specimens. Important techniques include high-resolution imaging (HREM), selected area electron diffraction (SAED), X-ray energy dispersive spectroscopy (XEDS), and electron energy loss spectroscopy (EELS). However, quantitatively understanding beam damage is necessary to realize the physical limitations of these cutting-edge techniques to study interfaces at a resolution required to gain understanding of material properties and electrochemical processes. Since the inception of electron microscopy, electron beam damage (and its mitigation) has been critically assessed (Egerton et al, 2004); (Baker & Rubenstein, 2010); (Jiang et al, 2015); (Zaluzec, 2019), and this will be discussed in the context of the damage mechanism identified for NBH in this paper.

Egerton divided mechanisms of electron beam damage into the primary classes of elastic (electron-nucleus) and inelastic (electron-electron) scattering (Egerton et al, 2004). Within these categories, displacement “knock-on” damage is strongly dependent on the energy of the incident electron beam, and below a threshold energy, the likelihood of displacement can become negligible (Bradley, 1988); (Bradley & Zaluzec, 1989); (Egerton et al, 2004). This elastic damage mechanism is not mitigated with cryogenic cooling. Inelastic beam damage stems primarily from mechanisms related to radiolysis, heating damage, and deposition of hydrocarbon contaminants. Radiolysis (sometimes referred to as ionization) is anticipated above 1 keV resulting in a damage rate proportional to the scattering events at each energy of the incident electron beam (Egerton, 2014). Imaging at cryogenic temperatures often offers the most significant benefit for mitigation in these materials by mitigating the thermal diffusion that propagates radiolytic damage (Bai et al, 2026).

In addition to the traditionally evaluated “knock-on” displacement and radiolysis damage mechanisms, an additional damage mechanism that persists in electronically insulative samples stems from electrostatic charging, in which the generation of secondary electrons can result in a surface charge (Cazaux, 1995, 1999, 2006); (Lin & Joy, 2005). This is demonstrated by the charge balanced equation, Equation 1, where electrons from the incident beam (I_0) can either 1) be backscattered, as described by the backscattered coefficient (η); 2) generate secondary electrons (SEs), quantified as the SE yield coefficient (δ); or 3) completely transmit through the sample of interest, measured as the transmitted current (I_t) (Cazaux, 2004). Here, η and δ are dimensionless coefficients relating the quantity of observed backscattered or secondary electrons to those delivered by the incident beam current, respectively. In cases when the sum of transmitted, backscattered, and secondary electrons deviates from the incident current, an excess of charge induces a local sample voltage (V_s) as mediated by the intrinsic electronic resistivity of the insulating sample (R_s) to preserve net charge balance, as the electrical resistance prevents electrons from the regions beyond the electron-beam interaction radius to ground the sample.

$$I_0(\eta)+I_0(\delta)+I_t-I_0=\frac{V_s}{R_s} \quad (1)$$

Electrostatic charging damage has been documented in glasses and lithium-based solid electrolytes to cause migration of alkali metal ions and result in their precipitation on the surface

as metals (Cazaux, 1993); (Jiang et al, 2007); (Jiang, 2012); (Jiang 2015); (Peng et al, 2021); (Liang et al, 2020). Owing to the electron beam having a probability for both elastic and inelastic interactions with the sample, damage mechanisms often compete and can result in varying predominant damage rates across various imaging conditions (Peng et al, 2021).

Herein, we present a series of time resolved and correlated electron microscopy experiments to diagnose the beam tolerance of NBH and the mechanism of its destruction. We consider and compare the effects of beam energy, dose rate (d_{rate}), and temperature as well as present cases for the damage in TEM vs. SEM and acceptable electron dosage for future characterization of the NBH system and its interfaces.

Materials and Methods

Materials

Particles of NBH precursors and mixed anion NBH were dried in a glovebox antechamber under dynamic vacuum at a temperature of 175 °C for 72 hours and then stored in a sealed container within an argon atmosphere glovebox (<0.1ppm H_2O and O_2). The mixed anion NBH was prepared from precursors following the procedures of Deysher et al (Deysher et al 2022). A 200-mesh copper grid with lacey carbon (no formvar) was dropped into a vial with the powder and cocktail shaken (with agitation and rotation) for five minutes to disperse particles onto the grid.

Transmission electron microscopy

Analytical Transmission and Scanning Transmission Electron Microscopy (TEM/ STEM), X-ray Energy Dispersive Spectroscopy (XEDS) and Electron Energy Loss Spectroscopy (EELS) measurements in this study were conducted using the Analytical PicoProbe Electron-Optical Beam Line / Iliad Ultra Scanning Transmission Electron Microscope at Argonne National Laboratory (Zaluzec, 2021). The prepared grids were then loaded into the Simple Origin Model 201 inert gas transfer cryogenic TEM holder (Figure S1) whereupon the tip was sealed within the argon gas atmosphere. The holder was then removed from the glovebox via the antechamber and inserted into the TEM column in the room next door after cleaning the external O-ring (< 3 minutes). The tip of the holder was opened to the airlock antechamber once the pressure gauge was below $1.0x10^{-5}$ torr in the pumping sequence and the holder was fully inserted to the column once the pressure gauge was below $3x10^{-6}$ torr. All operations within the microscope were conducted below $2x10^{-8}$ torr in the column.

Imaging reported herein was conducted at 60, 80, 200 and 300 keV using High Angle Annular Dark Field (HAADF), and Bright Field (BF) STEM using the microscope integrated Panther detectors. Phase Contrast Bright Field conventional TEM image and electron diffraction data were collected on the post column Ceta II CMOS 4kx4k and Falcon IV cameras. Observations were conducted at room temperature (RT) (23 °C) and as appropriate under cryogenic (-168°C) modes. XEDS hyperspectral images were collected using the XPAD detector (UltraX prototype) at 300 keV (Zaluzec, 2021). Calibrated doses were achieved by accurate control of beam diameter and beam current. Whilst multiple reproducible experiments were conducted, herein we detail an exemplar TEM + SAED measurement conducted on a mixed anion NBH particle by a 1 µm diameter probe with 100 pA probe current at 300 keV. A dose rate (d_{rate}) of ~8 e^{-} $Å^{-2}$ s^{-1} was

used throughout this experiment as measurements iterated between TEM and SAED modes at different locations along the particle. To capture changes dynamically, digital images (frames) were recorded every 500 ms. The diffraction dose study from 60-300 keV at room temperature and cryogenic mode employed a dose rate d_{rate} 2 e^{-} $Å^{-2}$ s^{-1} for NBH and sodium. In contrast, a d_{rate} of 20 e^{-} $Å^{-2}$ s^{-1} was able to be usede for LiF dose experiments due to their comparative robustness under the electron beam, The damage mechanism for LiF has already been studied in depth by Bai et al (Bai et al, 2026). During STEM imaging and hyperspectral XEDS or EELS measurements calibrated electron beam currents of 100 pA were employed while probe sizes and operating modes were varied as appropriate to the spatial resolution and dose required while dwell times of 0.8 ms/pixel were used. Tomography series data in these experiments were recorded using Thermo Fisher Scientific TOMO-5 software with a dose symmetric acquisition scheme of 6º increments (i.e. 0º, 6º, -6º, -12º, 12 º… 60º). Each tilt recorded and integrated the net XEDS signal of two 256x256 pixel frames (Comet et al, 2024). Hyperspectral STEM+EELS imaging used a dispersion of 0.072 eV per channel on the EELS Zebra detector.

Through a combination of low-dose low magnification TEM imaging and SAED, a freshly grown sodium particle was tilted to a zone axis with the interface positioned for HREM. A pre-aligned HREM field emission gun register was then loaded to the microscope for observation of the sodium | NBH interface at a d_{rate} of 20 e^{-} $Å^{-2}$ s^{-1} and a frame recording period of every half second. Drift correlated frame integration in Velox of five 0.5 s frames was used for HREM images of the sodium crystal interface with an NBH particle.

Throughout, no significant hydrocarbon contamination was observed that would affect image or spectroscopy measurements.

Scanning Electron Microscopy

SEM-focused ion beam (SEM-FIB) studies were conducted on a Thermo Fisher Scientific Aquilos-2 dual beam from 1 kV to 20 kV across a range of currents listed in the SI at both room temperature and cryogenically cooled to -171°C. Pellet samples were prepared from the NBH dried powders and uniaxially pressed for three minutes at 100 MPa (Deysher et al, 2022); (Deysher et al, 2024); [1,2]. Pellets were then extracted and fixed to an SEM stub with double sided carbon tape and inertly transferred from the glovebox to the microscope using a Thermo Fisher Scientific quick-connect transfer system. An Everhardt Thornley detector (ETD) secondary electron (SE) detector was used for imaging measurements. A consistent field of view of 17 µm x 12 µm was used for experiments at all beam conditions with a 1536 px by 1024 px frame size at a scan speed of 500 ms per frame. The experimental conditions were first tuned on a control area of the sample where sodium was already grown to ensure that the contrast range would be adequate to prevent substantial saturation in later frames. A low magnification image would be taken at the start and end of each experiment to observe changes outside the field of view. As with the TEM results, these experiments were also reproduced with identical experimental parameters and conditions to collect SEM + XEDS in a Scios-2 Cryo SEM-FIB. Crystals were grown under the same conditions and then XEDS spectrum line profiles were collected at 5 keV, 1.6 nA.

CASINO Simulations and Electron Yield Calculations

The Monte Carlo program CASINO 3.3.0.4 (Demers et al, 2011) was used to model numerous processes within this study in order to elucidate the mechanisms which we hypothesize electron beam damage. The CASINO simulations input parameters included the density of the NBH pellet 1.2g cm^{-3} and in addition, the compositional formula Na_4B_{22} was implemented as CASINO is not capable of calculating SE yield for hydrogen containing compounds.

For approximation of the yield curve of electrons escaping from the surface of NBH. We first describe functions for the electron penetration depth R and the inelastic mean free path of electrons (λ_{MFP}). R, was calculated with the Kanaya Okinawa range formula (Equation 2) across the range of 1-20 keV incident electron energies (E_0) (Kanaya & Okayama, 1972).

$$R = 0.\frac{0276 * A\, E_0^{1.35}}{Z^{0.89}\rho} \quad (2)$$

The values applied include an average atomic weight, A = 7.33 g/atom, the effective atomic mass Z for NBH of 6.407 amu and the density, ρ =1.2 g cm^{-3} which was determined via experimental measurement of a densified pellet.

The function for λ_{MFP} of electrons with respect to incident energy in NBH were derived from the method in Malis et al. with Equation 3 (Malis et al, 1988).

$$\lambda = \frac{106\,\tau\, E_0}{E_1 \zeta * \ln\left(\frac{2\beta E_0}{E_1 Z}\right)} \quad (3)$$

Where τ is a relativistic correction factor, E_1 is the critical energy for SE generation to occur, *ζ is* the critical energy barrier for secondary electron generation to occur in the system and β is the collection angle. There are many other models in literature by which λ_{MFP} of materials can be approximated (Tanuma et al, 1994). The Malis model was selected for our approximation as NBH fails to meet the criteria for application of the TPP-2M model for λ_{MFP} due to the following combined properties resulting in an invalid negative coefficient (Zemek et al, 2009). The combination of properties including density (1.2 g cm^{-1}), band gap (estimated to be 5.78 eV using DFT calculations with Heyd-Scuseria Ernzerhof exchange-correlation DFT calculation where the atoms and volume are relaxed within a cubic lattice (Heyd et al, 2003)) and plasmon energy (16 eV by TPP-2M estimation and 20.7 eV experimentally) along with delocalized electrons over the hydroborate cages are ill suited for the TPP-2M model.

The approximations of R and λ_{MFP} were combined to extract an electron yield curve, δ + η, as a function of incident beam energy in using Equation 4 for SE yield used by Seiler (Seiler, 1983).

$$\delta+\eta=\frac{B\lambda E_0}{R\zeta}\left(1-e^{\frac{-R}{\lambda}}\right) \quad (4)$$

B is a constant representing the likelihood of escape for an electron from the surface and is << 1.

Results and Discussion

Beam Damage in TEM and STEM

To understand the mechanisms of beam damage for this NBH solid-state electrolyte, a series of electron imaging, spectroscopy, and diffraction experiments were conducted on particles of NBH as synthesized via ball-milling (Deysher et al, 2022). Particulate samples were prepared within an argon gas glovebox and inertly transferred to the TEM (confirmed by Figure S1). To illustrate the mechanisms associated with damage in this system an exemplar data set (taken from a series of 344 measurements) is presented next. Figure 1, (supplementary Video 1), follows in detail the evolution of a single particle of NBH during three stages of its transformation. Before beginning the first stage, the NBH particle was carefully imaged in low-dose TEM (< 0.5 e^{-} $Å^{-2}$), (Figure 1a) and demonstrated a lightly faceted morphology with diffraction contrast and blunted edges.

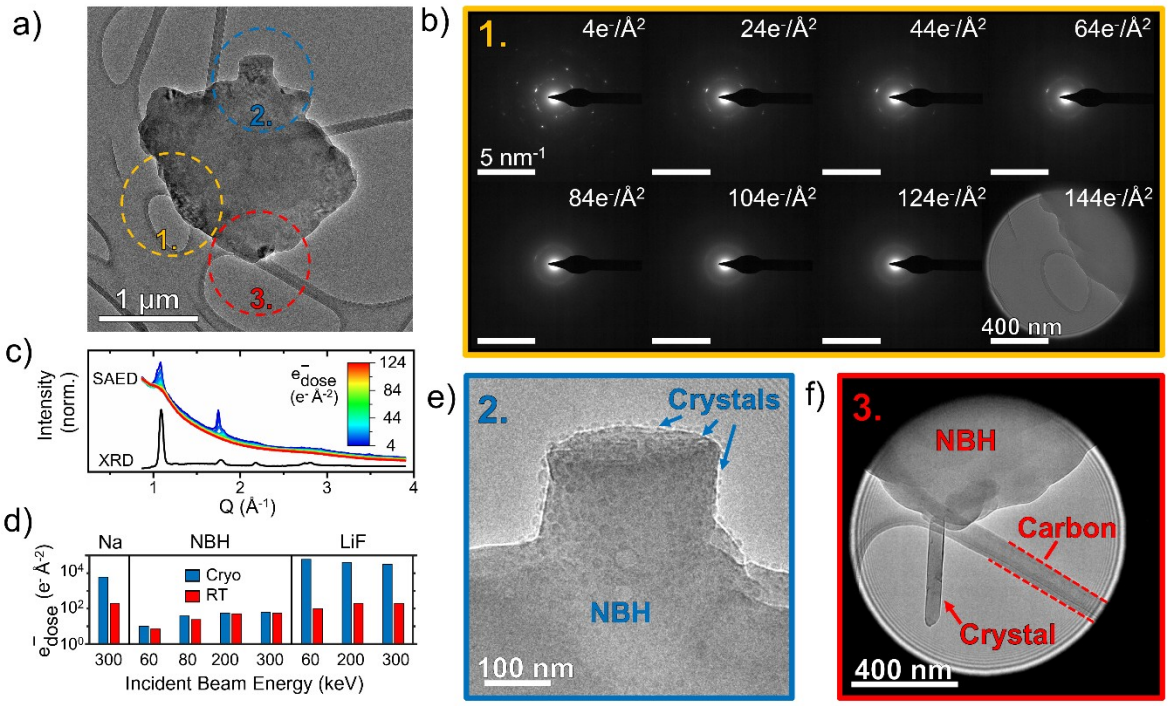

Fig 1. Low electron dose resolved TEM and SAED experiment for NBH irradiation damage. a. Low-dose TEM image of crystalline $Na_2(B_{10}H_{10})_{0.5}(B_{12}H_{12})_{0.5}$ particle. Three regions of sequentially staged experiments conducted on the same particle and described herein are circled. All three stages were conducted at 300 keV, room temperature, 100 pA and 1 µm probe diameter for a d_{rate} of 8 $e^{-}Å^{-2}s^{-1}$. b. Diffraction experiment sequence conducted as stage 1 [yellow

circle]. c. Radial integrated diffraction profile from the SAED experiment (c) compared with capillary XRD acquired with Mo K alpha radiation. d. SAED electron dose stability comparison of sodium metal, NBH and LiF at room temperature and cryogenic liquid nitrogen temperature across a range of energies. e. Stage 2 [blue circle] small crystal nuclei on opposing sides of the NBH particle from the diffraction experiment site. f. Stage 3 [red circle] large crystal nucleation at the contact point between NBH and lacey carbon TEM grid.

Alt text: a. Overview low dose TEM image of NBH particle on a lacey carbon TEM grid with three 1 µm regions highlighted around the particle edges. b. Seven panels of SAED in the first region, progressively losing diffraction contrast, the eighth panel is showing TEM of the region after diffraction contrast is lost. c. Plotted radial integration of the SAED profiles from (b) in Q space, compared with XRD. d. Bar plot comparing beam dose tolerance of sodium, NBH and LiF at various beam energies and temperatures. Cryogenic temperature improves tolerance for sodium and LiF but not as significant impact is seen for NBH. e. Small crystalline particles on the surface of NBH. f. two large crystals grown near the contact between NBH and the lacey carbon TEM grid.

The experimental evolution of the identified NBH particle then commenced at a constant d_{rate} of 8 $e^- Å^{-2} s^{-1}$ throughout the next three stages, where different regions of the particle were examined in both TEM and SAED with a time resolution of 0.5 s (supplementary Video 1). During stage 1, time-resolved SAED patterns (Figures 1b, c) were obtained on the region of the particle labeled 1 in Figure 1a. Additional frames are included in Figure S2. These SAED patterns demonstrated the crystalline nature of the NBH particle and quantitatively agreed with bulk XRD measurements (Figure 1c), indexed to the previously reported FCC crystal structure (Duchêne et al, 2017). During further time-resolved data acquisition, the NBH particle quickly amorphized from beam-induced damage. Diffraction reflections at nominally larger scattering vectors (e.g., smaller d-spacing) were observed to decay more rapidly. Beyond 84 $e^- Å^{-2}$ SAED patterns demonstrated only a broad amorphous ring at 1.7 nm^{-1} (d-spacing of 5.9 Å).

To investigate the impact of imaging conditions on the rate of beam damage and consistency of the damage mechanism, SAED and imaging studies were repeated with varied incident beam energies of 60, 80, 200, and 300 keV, at both ambient and cryogenic temperatures (Figures S5, Table 1). Quantitative results from these studies are shown in Figure 1d, which compares the total dose sustained by NBH particles before amorphization at various imaging conditions. As made necessary by the dose stability of NBH at 60kV of just 7 ± 2 $e^- Å^{-2}$, all experiments for NBH and sodium were conducted between d_{rate} of 1-2 $e^- Å^{-2} s^{-1}$ to ensure detection of the amorphization dose. LiF, exhibiting higher beam tolerance benefit from cryogenic temperature, was studied separately at a d_{rate} of 20 $e^- Å^{-2} s^{-1}$. The monoclinic precursors of $Na_2B_{10}H_{10}$ and $Na_2B_{12}H_{12}$ were similarly examined in Figure S3, Table 2 at 300 keV for both room temperature and cryogenic temperature. The same trend holds true albeit $Na_2B_{10}H_{10}$ possesses the highest beam tolerance.

Increased electron beam energy offers greater stability of NBH under the electron beam (e.g., longer time-to-amorphization) as shown in Figure 1d. Additionally, cryogenic temperatures resulted in only minimal benefits toward preserving the crystallinity of the NBH particles in

contrast to other beam-sensitive battery materials (i.e., Li, Na, and common SEI components such as LiF, Li_2CO_3, and NaF) where elastic damage was observed to dominate signified by mass loss occurring in tandem with morphology change (Bai et al, 2026).

After stage 1 which focused on the evolution of SAED, stages 2-3 of this exemplar, time resolved imaging was used to evaluate the resulting implications of NBH beam damage in TEM over time with a continued d_{rate} of 8 $e^- Å^{-2} s^{-1}$. The large NBH particle had experienced a d_{total} of 220 $e^- Å^{-2}$ when many small particles (< 10 nm diameter), not previously present in the low dose overview image, emerged and coated the surface of the NBH SSE (Figure 1e). These small particles rapidly damaged by the electron beam via displacement damage which is markedly different from the damage to the NBH. These particle cores experienced mass loss simultaneously with their loss in crystallinity, leaving behind shells that then were destroyed by the irradiation. By d_{total} of 200 $e^- Å^{-2}$, only the NBH particle remained (supporting frames shown in Figure S4). Terminating this imaging sequence, the contact point of the NBH particle with the lacey carbon TEM grid (region 3 in Figure 1a) was investigated. Here, large sodium crystals (as indexed via SAED supplementary Video 1, Figure S5) emerged from this contact point. Contrasting with the small uniform coating of crystals in region 2, this contact point region only contained two crystals with comparatively large projected lateral dimensions of 200 nm and 400 nm. The noticeable difference between stages 2 and 3 in this exemplar is the presence of the carbon grid. Here it is hypothesized that, after migrating through NBH in response to a positive local charge, sodium ions that reach the contact point with the carbon TEM grid are reduced to sodium metal at kinetically favorable rate to grow large crystals due to the relative abundance of available electrons from the carbon grid. Comparatively, sodium ions reaching the surface of the NBH that extends into vacuum encounter a deficiency of available electrons resulting in no preferential single nucleation site.

In summation, these reproducible observations suggest that NBH solid electrolyte undergoes a damage mechanism due to electron-irradiation that 1) amorphizes the bulk NBH solid electrolyte particle without morphological damage and 2) results in growth of crystalline particles on the surface of the NBH that evidence suggests are nominally sodium metal. Such metal sodium expulsion occurring in the periphery of the transmission electron beam is consistent with the description of electrostatic beam damage by Jiang (Jiang, 2016).

In addition to the structural details provided from SAED and TEM imaging, spectroscopic techniques (e.g., XEDS and EELS) were employed to obtain elemental insights on the in-situ grown particles and further inform the mechanism of beam damage. In a complementary set of experiments, TEM imaging was conducted in area labelled “1” in Figure 2a. Consistent with the exemplar, imaging in this region was accompanied by a loss in diffraction contrast from electron-induced beam damage. Following this TEM imaging (and beam damage), a STEM XEDS hyperspectral image was acquired (Figures 2a, b). The bright field image, shown in Figure 2a, and the comparison of the boron and sodium K edge-filtered images in Figure 2b, indicate three distinct and representative regions resulting from electron-beam induced damage. The damaged area, which was exposed to a TEM probe (region 1 labeled in Figure 2a), is devoid of sodium K signal in the XEDS hyperspectral images. Meanwhile, the boron K signal and particle

morphology are retained in this region. In contrast, beyond the radius of irradiation by the TEM electron probe (representative region 2 labeled in Figure 2a), signals from both the boron and sodium K coexist as expected for the pristine NBH stoichiometry. Additional needle-like structures (labelled region 3 in Figure 2a) were also identified, where signal from the boron K was lacking and instead intensity derived from sodium K. Further quantitative confirmation is shown in Figure 2c, which compares the resulting XEDS spectra from these distinct representative regions. In addition to the boron and sodium K shell signals, small amounts of carbon and copper are detected and can be attributed to system peaks from the TEM grid. Together, these results further confirm the ejection of sodium metal from the bulk to the surface of the NBH solid electrolyte after damage from a focused electron beam.

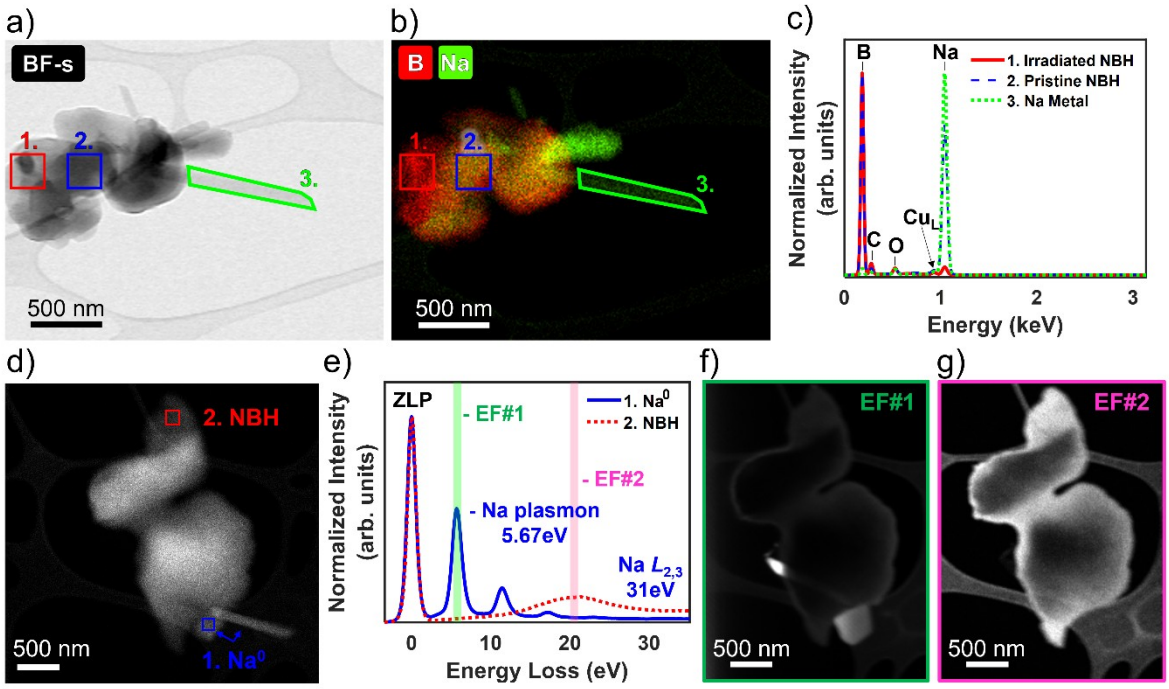

Fig 2. Spectroscopic studies of NBH electron irradiation damage a. Bright field STEM image of the NBH particle on the lacey carbon TEM grid with green blue and red overlays of selected areas integrated into XEDS spectra displayed in (2c). Data collected at room temperature, 300 keV, 100 pA and 1 ms/pixel. Left area was exposed to the electron beam for TEM study and recorded reduced sodium K shell signal intensity. The center region of the particle is comprised of bulk NBH. Right side features sodium crystals grown from the contact point of NBH particle and the carbon TEM grid. b. Boron and sodium XEDS hyperspectral image (HSI) of NBH particle and sodium crystal growths. HSI is comprised of the net signal of six integrated frames. c. Extracted spectra from the selected areas in (a). d. HAADF STEM micrograph pre-EELS Hyperspectral Image acquisition with two sodium crystals grown. e. Two low-loss energy spectra from the hyperspectral image integrating 1000 frames: Blue, lower corner, Metallic plasmon signature matching the literature values for sodium metal with the primary peak at approximately 5.67 eV. faint sodium $L_{2,3}$ at 31 eV. Red, no metallic plasmon signature with initial low loss peak near 20.7 eV. Energy filtered (EF) images for the (f) sodium plasmon and (g) NBH

low loss peak were extracted from the spectrum image and clearly segment the sodium crystal from the SSE particle.

Alt text: a. STEM bright field overview of particle with 3 subregions. b. XEDS spectrum image at same magnification as a., demonstrating that the three regions have different intensities for Na and B signal. c. Plot of the three subregions integrated spectra, region one has intense boron weak sodium, region 2 is similar intensity of boron and sodium, region 3 has weak boron and intense sodium. d. STEM HAADF overview of another particle with 2 subregions over the bulk particle and a grown crystal. e. Low energy loss spectra for the two subregions in (d) f. Energy filtered image of the sodium plasmon, intense signal on the grown crystal particles. g. Energy filtered image of the bulk NBH plasmon matches the original NBH particle morphology with no intensity of the grown particles.

To further confirm the faceted growths as metallic sodium particles, STEM HAADF imaging (Figure 2d) and EELS hyperspectral imaging (Figures 2f, g) were employed. Before detailed spectrum imaging, HAADF STEM imaging of a NBH particle initiated the growth of two bright faceted particles (Figure 2d). Compared, in Figure 2e, are low-loss spectra from the sodium particle (region 1 in Figure 2d) and from the bulk NBH particle (region 2 in Figure 2d). Here, the spectrum obtained from the faceted particle clearly exhibits characteristic plasmon peaks of sodium metal at 5.67 eV and successive multiple plasmon loss ($\delta E \sim 5.7$ eV) peaks at incrementally increased energy loss, confirming the damage-induced growths as sodium metal in conjunction with SAED from Figure S2 (Jiang et al, 2008); (Yang et al, 2021). In comparison, the spectrum from the NBH particle exhibits only a broad peak near 20.7 eV in the low-loss EELS region. As a result, spectrum images were mapped of the first sodium plasmon peak and the low-loss peak from NBH to clearly distinguish the sodium crystals from the solid electrolyte. Over the course of the EELS spectral imaging, the needle-like sodium crystal moved from its original position in the HAADF scan in Figure 2d to flip in orientation and overlap with the solid electrolyte particle in Figure 2f, although the more cubic crystal neighboring it remains where it originated. The NBH EELS spectrum image in Figure 2g exhibits inhomogeneous intensity due to thickness effects near the center of the two main particles where the relative log-ratio thickness of our particle, t/λ approaches 5. Thicknesses, t, greater than 1 indicate that λ_{MFP} of an electron transmitting through the sample is expected to experience significant multiple scattering events (Malis et al, 1988).

The preceding results rely on *ex-situ* growth of the sodium crystal on the opposing ends of the particle in a “hide and seek” fashion. To expand control over our understanding of the sodium expulsion into different sites and sizes, we additionally captured the growth of sodium crystals with another technique. While traditional TEM and STEM experiments capture 2D projections, the evolution of 3D morphology is logically required to confirm our hypothesis that the large crystals extrude from the contact point with the grid in relation to charging damage. Therefore, STEM+XEDS tomography with ± 60° tilt was also conducted the results from which (Figure 3, supplementary Video 2) supports our hypothesis from the 2D projections The tomography experiment detailed in Figure 3 also highlights that, after expulsion of sodium from the bulk NBH initially grow as sodium metal crystals on the surface from beam damage, further electron

dose next results in sputtering of sodium metal which subsequently and progressively coats the neighboring carbon TEM grid.

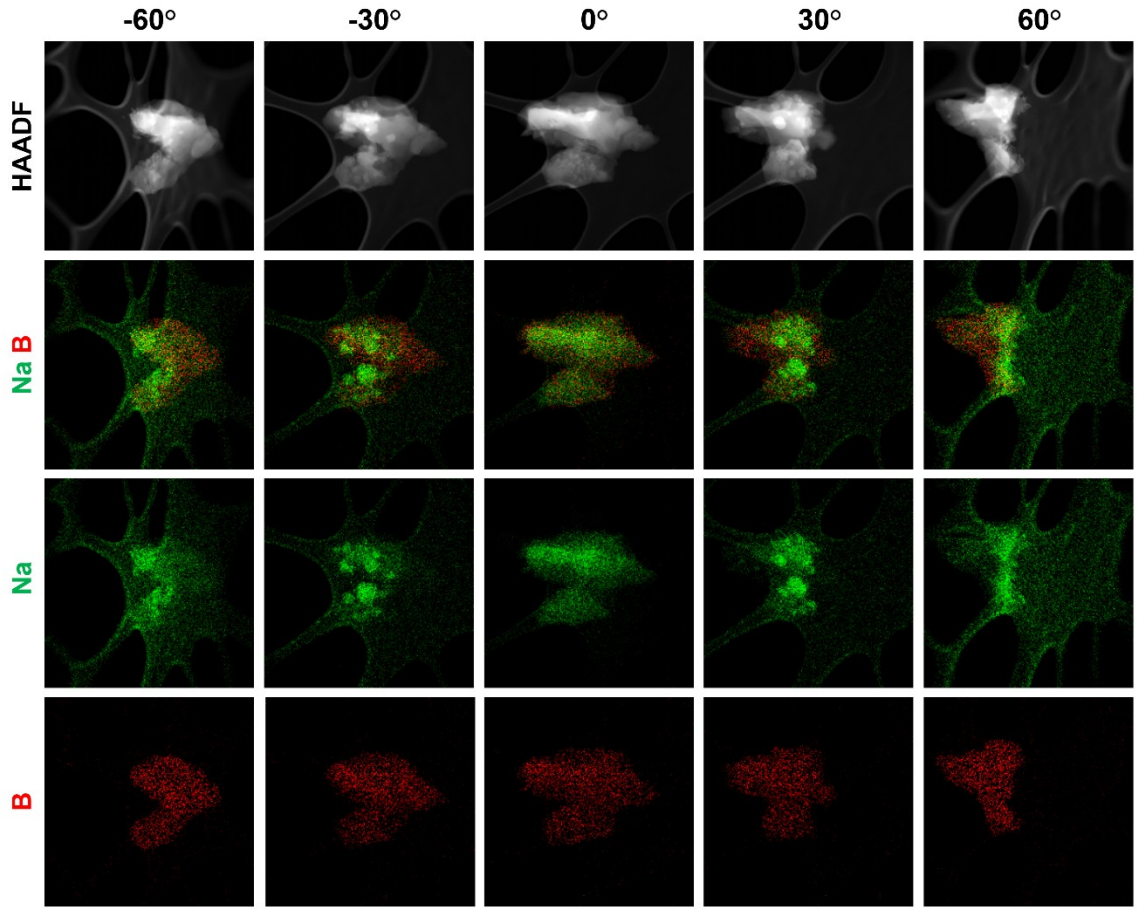

Fig 3. STEM+XEDS tomography sequence of NBH particle. Separate views of HAADF signal and integrated net signal spectra for sodium + boron, sodium and then boron are shown every 30°. Middle column was acquired first in the acquisition schema.

Alt text: Four rows of five images at intervals of 30º. Each row is a different signal, HAADF, sodium + boron, sodium and boron from top to bottom. The HAADF and sodium signals display changes over the course of the series. Particles grow on the original particle (brighter in HAADF intensity and in sodium counts). The boron signal maintains the original particle morphology and intensity from the initial image at 0º throughout the series.

With the ability to tomographically hyperspectral image these large sodium metal crystals interface with NBH, we additionally can probe the interface for a solid electrolyte interphase and glean an understanding of the dose dependent evolution. To explore this, Sodium metal was grown under low dose conditions of 8 $Å^{-2}$ s^{-1} from the opposing side of a NBH particle (with the same procedure as the exemplar). Using HREM mode in TEM, it was also possible to observe a crystal lattice having a periodic spacing of 3.02 Å which correlates to the sodium (110) predicted spacing (Figure 4a-c). The NBH appears non-crystalline at this orientation/ magnification with the only periodicity from the sodium crystal in the fast Fourier transform (FFT) (Figure 4c).

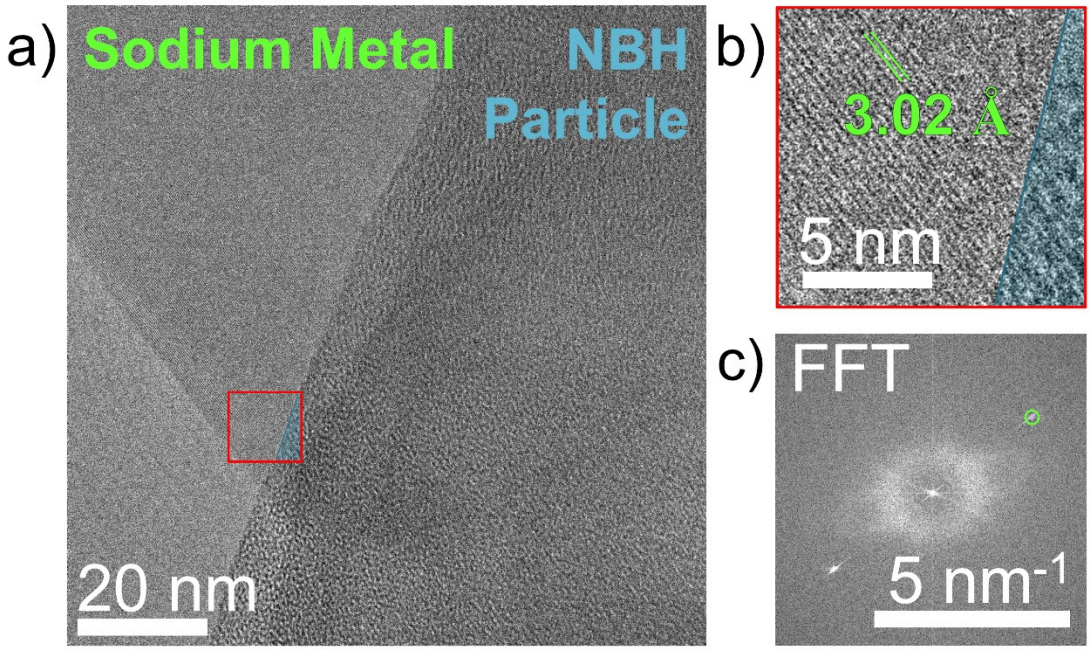

Fig 4. HREM of sodium and NBH interface. a. Drift correlated frame integrated image at the NBH particle | sodium metal interface, recorded every 0.5 s at d_{rate} of 20 e^{-} $Å^{-2}$ s^{-1} for 2.5 seconds for d_{total} 100 e^{-} $Å^{-2}$. Pixel size is 49.55 pm. b. Digitally magnified interface. c. The FFT of the micrograph.

Alt text: a. A high-resolution image of grown sodium on the surface of NBH. b. An inset from the main figure showing the periodic spacing of 3.02 Å. c. The FFT of a. only has one pair of periodic spacing resolved and a diffuse amorphous ring.

The compendium of this data clearly demonstrate a consistent damage mechanism induced by a focused electron beam, wherein 1) the bulk NBH solid electrolyte loses sodium content and crystallinity; 2) faceted, crystalline, metallic sodium particles are grown on the surface of the NBH, with a strong preference toward grounded contacts with the TEM grid; and finally 3) metallic sodium metal growths are further damaged via sputtering with resulting dispersal across the TEM grid support. The change observed that the primary physical origin of beam damage in NBH is inelastic from electrostatic charging as opposed to displacement damage or radiolysis, which would result in significant morphological changes. Further, the lack of effectiveness of cryo-protection nor reduction of beam energy for increasing NBH beam tolerance is consistent with previous observations of electrostatic charging beam damage of other electronic insulators, including solid electrolytes (Jiang et al, 2007); (Peng et al 2021).

Beam Damage in the SEM

The TEM data, presented herein, was acquired with consistent imaging conditions but is limited in control over geometrical considerations that could influence the damage rate (e.g., incident beam angle and particle thickness) and overall beam tolerance. Therefore, SEM was additionally employed to further investigate the mechanism of electrostatic beam damage with controlled sample thickness and morphology. In contrast to TEM, in SEM the sample thickness eliminates

transmitted electrons from Equation 1, resulting in a limited penetration depth of the incident electron beam into the sample.

The complementary SEM dose study was conducted on the surface of a densified pellet of NBH which was subjected to a constant rate of irradiation by the electron beam (supplementary Video 3, Figure 5a). Initially, and reproducibly, only small pores and impressions from the press are present on the surface of the pristine pellet (Figure 5a). No visible changes were observed until ~ 190s, after which time (and dose) bright features (confirmed to be sodium by XEDS in Figure S6) emerge from the surface at the site of a defect on (Figure 5b). Further electron irradiation resulted in growth of the sodium metal with a faceted morphology (Figure 5c) until apparent radiolysis subsequently damaged the sodium metal surface. By 300 s, additional perturbances appeared and grew on the surface and are seen in Figure 5d. These perturbances are the locations where subsequent sodium crystals emerged. The irradiated region was clearly visible with an expanded field of view (Figure 5e).

A focused ion beam (FIB) was then subsequently employed to create cross-sectional views through the irradiated region (Figure 5f, supplementary Video 4). The FIB rapidly damaged the sodium metal, however, as the cross-sectional slices approached the bulges, pores were revealed beneath the surface. The NBH electrostatic damage affecting crystallinity in this work contrasts with the topotactic reaction seen by Peng et al for Li growth from the LLZO solid electrolyte as LLZO retained its crystalline structure during alkali metal expulsion (Peng et al, 2021).

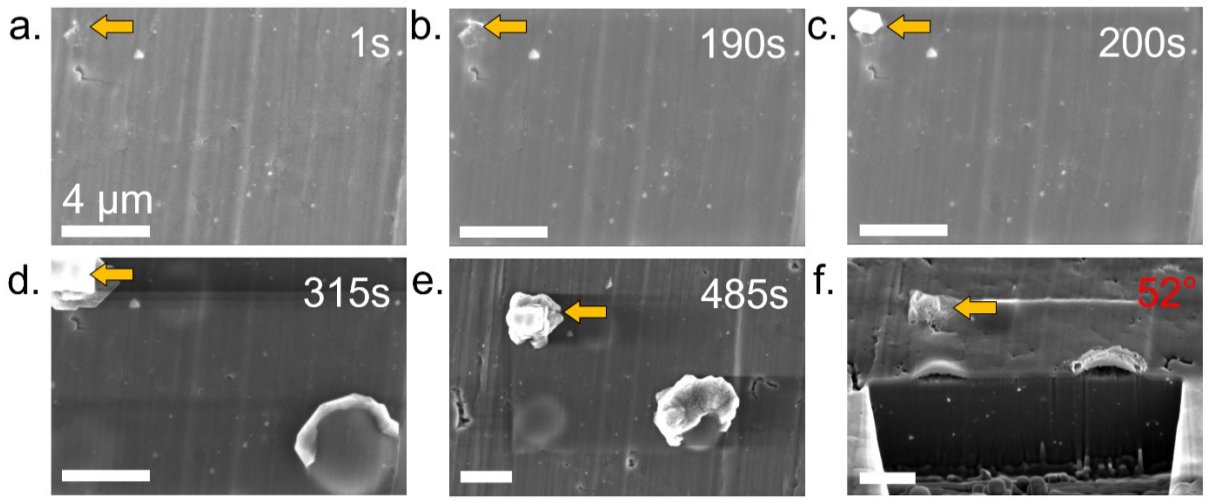

Fig 5. Inert transfer Cryo-SEM damage experiment of a mixed anion NBH pellet 5kV, 1.6nA and 500 ns pixel^{-1} with a field of view of approximately 12 µm x 17 µm. (See supplementary Video 3) a.-b. The sample appeared unchanged for 190 s. c. At 200 s, a faceted sodium crystal extruded and grew from the surface. d. Surface perturbances became apparent and then burst after 300 s. e. After approximately 500 s, we demagnify to reveal that the electron beam dosed region has swollen. Several perturbances have grown on the surface. f. Next, cross sections of the dosed area were revealed with a Ga^+ ion beam 30 kV, 2.7 nA (See supplementary Video 4). All scale bars 4µm.

Alt text: a.-f. A series of 5 SEM micrographs of the same region of NBH at selected time intervals where changes are observed with bright crystals emerging from the surface. An orange arrow points to the same location in each image where the first crystal emerges from and grows. The fifth image (g.) is at a wider field of view to observe changes including charging contrast change for the irradiated region. g. The revealed cross section of the irradiated NBH.

Analogous SEM experiments to Figure 5 were conducted at both cryogenic and room temperature with various beam currents and beam energies in the SEM (results in Figure 6a-b, and Figure S7-10, Table 3-4). Comparing first, the effect of beam current on the time required for sodium expulsion at 5 keV (Figure 6a), lower currents have greater beam tolerance. At 0.4 nA NBH is stable for almost 607 s at room temperature while increasing the current exhibits a severe negative correlation causing sodium to appear faster and from more nucleation sites. For the largest current employed (26 nA), sodium is expelled from the surface in just 9 seconds. This trend is in agreement with the expectation that charging and radiolysis scales with electron flux (Egerton, 2014).

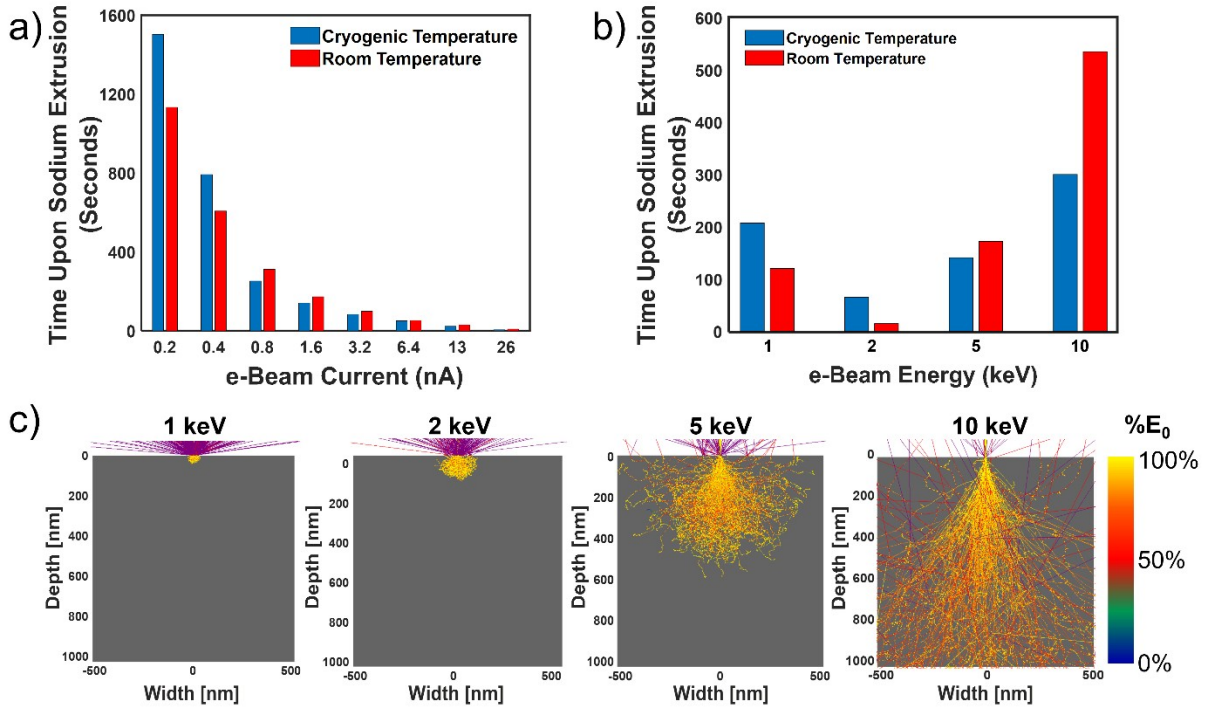

Fig 6. Time until damage matrix for SEM dose experiments and simulated yield from Monte Carlo mirrors of the evaluated SEM beam energies. a. SEM dose experiment matrix comparing the time upon sodium extrudes from the surface of the NBH at varied beam currents and temperatures. b. Similar SEM dose experiment matrix evaluating the effect of e-beam energy and temperature. c. Displays electron dispersion for 1, 2, 5, and 10 keV CASINO Monte Carlo simulations of a 5 μm^3 volume (magnified to 1 μm^3) of NBH.

Alt text: a. Bar plot showing that lower beam currents take longer to cause sodium to grow from the surface in SEM, Cryogenic temperatures are better than room temperature at low currents but

worse from 0.8 nA to 26 nA. b. Bar plot showing that the worst e^- beam energy for fast sodium growth is 2 keV. This energy also serves as an inflection point for the benefit/ disability of cryogenic protection of NBH from sodium ejection. c. A series of four cross sectional electron trajectory simulations created in CASINO at the e^- beam energies of b. the interaction volume increases dramatically with increasing energy.

Compared to the impact of beam current, the impact of changing beam energy between 1 keV, 2 keV, 5 keV and 10 keV in Figure 5b and in changing between cryogenic vs room temperature was more complex to analyze.

Discussion and Analysis: TEM, STEM, and SEM Beam Damage

To better understand how incident beam voltage and sample temperature influence beam damage, we must understand the possible effects on the probability of SE generation and also yield from the surface.

Monte Carlo (MC) simulations described previously of electron trajectories were employed as a first approximation to determine the interaction volume of the electron beam with the bulk NBH sample across 1-10 keV (Figure 5C). Given elemental composition, density (experimentally measured 1.2 g cm^{-3}, plasmon energy 20.7 eV, and simulated work function 6.75 eV) CASINO V3.3.0.4 can estimate the ratio of transmitted, backscattered (BSE, η), and secondary electrons (SE, δ) at a surface (Demers et al, 2011). Following the principles of charge balance and assuming negligible electronic conductivity (Equation 1), the generation of BSE and SE at proportions greater than the incident beam results in the accumulation of a net positive local charge. However, it should be noted that this version of CASINO is limited in handling the proper generation of secondary electrons produced in hydrogen containing compounds and for the compensation of delocalized electrons among the borohydride cages.

The utility of the CASINO simulations in Figure 6c is in representing the influence of changing incident beam energy, I_o, on the interaction volume of the electron beam with NBH calculated using the Kanaya Okinawa formula (Equation 2) (Kanaya & Okayama, 1972). The resulting R as a function of energy in Figure 7a matches with the CASINO simulated penetration depth in Figure 6c with values of R = 30 nm and 102 nm, respectively, at 1 and 2 keV. These values already help demonstrate the main consideration of variance between SEM and TEM experiments. The thickness of our SEM sample ($\geq$ 800μm) is vastly greater than the penetration depth, R, of the SEM incident electron beam whereas our particles in TEM can expect transmission of a majority of the electron current. Next in the pathway to establishing a yield curve, we approximated the probability of generated secondary electrons reaching the NBH surface in order to escape, based upon the λ_{MFP} in Figure 7c. Combining R and λ_{MFP}, we estimate the yield, $\delta + \eta$ in Figure 7c. The yield curve has 3 regimes representing charging cases, Initially, below 1 keV, $\delta + \eta < 1$ which would result in negative charging of the particle. Between 1 – 13 keV, $\delta + \eta > 1$ predicts positive charging of the interaction volume from excess SE generation. Beyond 13 keV, $\delta + \eta$ drops below unity again. It should be noted that these yield curves do not account for the buildup of charge gradients with time in insulators and are instead an instantaneous evaluation leaving the possibility of delayed positive charging.

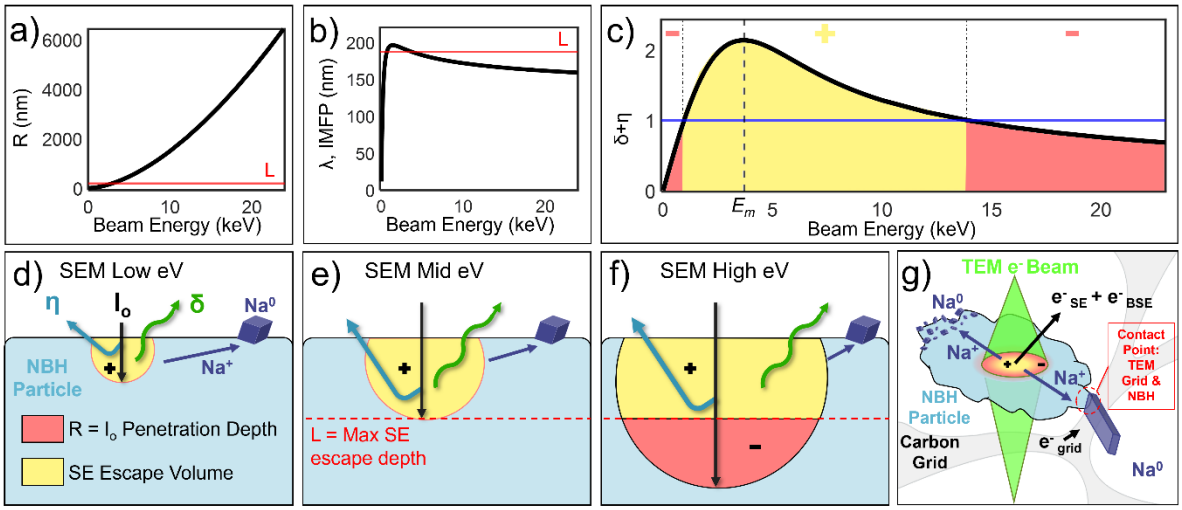

Fig 7. Calculations for electron yield curve and the resulting schematic models of electron beam interaction with NBH. a. R as a function of incident beam energy into NBH. b. Inelastic mean free path of electrons through NBH as a function of electron beam energy. c. Approximated standard yield curve for NBH as a function of beam energy. d. Schematic for low I_o. e. Case for R ≈ SE escape volume f. Case for R >> SE escape volume. g. Schematic for TEM electron bias of a thin sample at high keV and the resulting motion of electrons and sodium ions through the sample.

Alt text: a. Calculated electron beam penetration depth, increases with energy. b. Inelastic mean free path has an inflection at low energy. c. Electron yield curve for NBH, a yellow color representing the conditions for instantaneous positive charging at the surface, pink representing conditions for instantaneous negative charging has a low energy and high energy regime. The maximum charging energy is a peak at 3.6 keV. d.-f. Schematics showing the changing scenarios for the SEM beam interaction with energy as penetration depth and the possibility of SE escape from that depth and the motion of Na^+ in response to the charging scenario. At high keV, a pink region represents regions too deep for SE escape. g. A schematic for TEM e^- beam interaction with NBH, driving Na^+ to grow into two different size crystals determined by contact with either the NBH surface or the carbon TEM grid.

Combining results from the experimental study and approximated yield curve for the three cases, one can summarize schematics for interactions of the electron beam I_o with NBH in the SEM (Figure 7d-f) and TEM (Figure 7g). As depicted in Figures 6d-f, the beam energy dictates the volume from which back scattered electrons η are generated and secondary electrons δ knocked out can escape from the surface. The energy distribution left behind by the excess SE will result in positive charging of the radiated region which, due to the sluggish electron conduction and lack of charge dissipation, results in the expulsion of the positively charged sodium ions from the structure.

In contrasting the results of calculated values, one can understand the impact of beam energy on the sodium expulsion in the SEM by comparing the three charging scenarios for NBH. First, at

low E_0 (Figure 7d), the penetration depth is very small, and the small SE yield from this interaction volume is insufficient to create a large charge gradient in NBH. At intermediate E_0 in Figure 7e, the penetration depth approaches the maximum secondary electron escape depth, L. L is approximated to be close to λ_{MFP} at the maximum yield energy, E_m, in Figure 7c yielding a value of 126.2 nm (Cazaux, 2006).

Incident energies at the peak E_m of 3.6 keV will result in the maximum charging scenario by inducing the largest possible interaction volume that can contribute to local positive charging through SE yield. Beyond this E_0 (Figure 6f) additional energy results in SE generation deep in the bulk. Such SEs exhibit a low probability of escape. Thus, as incident energy increases further, the majority of SE are now generated too deep inside the bulk material to contribute to surface charging. This is why in the experiments illustrated in Figure 5b, above 2 keV, significantly increased cumulative electron dose was required for sodium expulsion to occur.

At a given current, electron beams with increased energy also exhibit a larger mean free path for electrons transmitted through the sample, thereby lowering the instances of inelastic collisions to generate secondary electrons for two different energy beams of the same current.

The value of E_m for insulators in literature is commonly around 2 keV but can vary in experimental data due to the influence of sample processing and geometry (Cazaux, 2006). The calculated E_m of 3.6 keV in Figure 6c is plausibly ranged in comparison to the trends of our experimental data in Figure 5b, which revealed the most rapid sodium expulsion from NBH at 2 keV. Variance in experimental data from theory derives from limited treatment of delocalized electrons and hydrogen-terminated hydroborate cages by central assumptions of Equations 2-4. The hydrogen terminated hydroborate cages, with two delocalized electrons, are expected to exhibit charging behavior under electron beam bias due to the long mean free path and large band gap energy. Another important distinction between simulation and experiment is the assumption of steady-state flow in contrast to the transient nature of charging during real experiments. Electronic conductors are able to alleviate the impended positive surface charge with electrons from the bulk, but electronic insulators are susceptible to enhanced charging by dose rate and not solely total dose of electrons.

Above 2 keV the conventional wisdom of lowering temperature to reduce damage does not apply as the expanded L enables faster charging of the sample. Knowledge of L additionally is useful in explaining the changing trend in the effect of temperature on the rate of sodium expulsion in the SEM dose experiments. The findings of Cazaux have previously related the increase in electrostatic beam damage at low temperatures to the decrease in electron-phonon interactions (Cazaux, 1993). This decrease would in turn result in an increase for the escape depth of electrons which expands the maximum possible volume of NBH contributing to charging raising E_m. The data trend for temperature in Figure 6b experiences the inversion at the same beam energy range trend inversion of 2-5 keV explained above. Consistency with the predictions in the damage beam tolerance trend across conditions of beam energy and temperature in Figure 6b for SEM and Figure 1d for TEM signify electrostatic charging as the predominant damage mechanism for NBH

In contrast to the SEM case, the TEM schematic of Figure 7g emphasizes that most of the electrons are transmitted through the solid electrolyte. As such, a cylindrical charging region in line with the radius of the electron beam will be formed. Collisions with the electron beam have ample energy to displace secondary electrons. As this core can immediately develop a local positive charge, sodium ions will rapidly migrate radially to balance the net charge of the sample. The sodium ions progressing to the surface of the NBH encounter two possible end results. First, sodium ions reaching the particle surface adjacent to the vacuum of the TEM column are seen to nucleate into a large number of small sodium crystals (Figure 1e), whereas sodium ions directed towards the contact point between the NBH and the carbon TEM grid are met at the interface by a grounded, rapidly replenished source of electrons. This contact results in favorable crystal growth kinetics from fewer nuclei similar to the result in Figure 1f. In studying the pathways of electrons and ions in the pursuit of maintaining charge neutrality, we have revealed the influence of electron probes on NBH SSE.

The NBH electrostatic damage observed in both SEM and TEM compares well with the electrostatic damage seen by Peng *et al.* for Li growth from the LLZO solid electrolyte (Peng et al, 2021). A distinctive difference remains though as LLZO damage was topotactic and retained its crystalline structure during alkali metal expulsion (Peng et al 2021). Within the scope of this study, we cannot definitively prove the charge compensation response of the hydroborate cages but these results strongly support our hypothesis and elucidation in follow up study. Under the influence of the locally induced high voltage conditions above the NBH oxidation potential of 3.2 V relative to sodium/sodium ion (Deysher et al, 2024), we suspect that the hydroborate $B_{10}H_{10}^{-2}$ and $B_{12}H_{12}^{-2}$ cages would oxidize (Paetzold et al, 2007); (Jin et al, 2024). We would further expect a complex reaction to occur for the mixed anion hydroborate cages. Advanced time-resolved EELS that can detect changes in the boron binding environment may elucidate this hypothesis, but the rapid structural changes recorded in SAED suggest that capturing this evolution could pose a serious technical challenge. Interpretation of the data would additionally require advanced simulation to compare and distinguish the features of interest within the spectrum that would represent such a bonding change in the hydroborate cages within a limited electron dosage across short time resolution.

Conclusions

Sodium *closo*-hydroborates represent an important class of sodium solid-state electrolytes owing to their appreciable ionic conductivity, favorable mechanical properties, and thermodynamic compatibility with sodium metal anodes that together enable anode-free configurations with efficient ion transfer. However, compared to other beam-sensitive battery materials such as sodium metal, studying these solid electrolytes with electron microscopes presents additional challenges outside of the dominant and well-known radiolytic damage mechanisms. While cryogenic EM aids the beam stability of alkali metal, NBH exhibits a primary damage mechanism of electrostatic charging due to excess secondary electron generation and low electronic conductivity that is not significantly mitigated by cryo-protection. Here, we show that NBH exhibits an onset of beam damage even before a dose of 10 e^{-} $Å^{-2}$, which results in complete

amorphization before 80 $e^{-}Å^{-2}$ at 300 keV. In response to positive charging by the electron beam, sodium metal was extruded from the bulk particle, either as small nuclei that coats the particle surface or as large, faceted crystals at grounded contact points between the NBH particle and the lacey carbon TEM grid. The interface between NBH and sodium displayed no significant chemical gradients in boron content nor featured an amorphous interlayer of distinct contrast supporting the conclusion that there is no SEI formation. A systematic search of beam energies found that an experimental maximum charging rate occurs at 2 keV with decreasing damage rates at higher energies. In conjunction with experimentation, Monte Carlo simulations and calculations support positive charging induced from secondary electron generation of NBH. Increasing voltage does not eliminate the damage mechanism but by increasing the interaction volume proportionally to the inverse electron wavelength, it decreases the charge per area prolonging stability with the increased resolution. From these studies, we strongly advocate and recommend that all EM studies of solid electrolytes undergo careful dose evaluation prior to making mechanistic conclusions about battery performance. Just as high-speed detectors with large signal-to-noise enabled these studies, the authors remain optimistic that single frame 4D-STEM offers an avenue for future imaging of beam-sensitive solid-state electrolytes, such as sodium hydroborates.

Acknowledgements

This work is funded by the Energy Storage Research Alliance "ESRA" (DE-AC02-06CH11357), an Energy Innovation Hub funded by the U.S. Department of Energy, Office of Science, Basic Energy Sciences. The work performed on Thermo Fisher Scientific Iliad Ultra was developed and supported as part of a CRADA #01300710 and CRADA #A24560 among Argonne National Laboratory, University of Chicago and Thermo Fisher Scientific. This research was also supported in part by the National Science Foundation Major Research Instrumentation (MRI) Program (NSF DMR-2117896) at the University of Chicago. This material is based upon work supported by the National Science Foundation Graduate Research Fellowship Program under Grant No. 214000.

Tables

Table 1. TEM amorphization dose for NBH across temperature and voltages.

Beam Conditions	Amorphization Dose ($e^{-}/Å^{2}/s$)	Std. Dev ($e^{-}/Å^{2}/s$)
300 keV RT NBH	54	7
300 keV Cryo NBH	61	5
200 keV RT NBH	51	6
200 keV Cryo NBH	56	10
80 keV RT NBH	24	6
80 keV Cryo NBH	38	5

60 keV RT NBH	7	2
60 keV Cryo NBH	10	4

Table 2. TEM amorphization dose for $Na_2B_{10}H_{10}$ and $Na_2B_{12}H_{12}$ precursors at 300 keV at room temperature and cryogenic temperature.

Beam Conditions	**Amorphization Dose ($e^-/Å^2/s$)**	**Std. Dev ($e^-/Å^2/s$)**
300 keV RT $Na_2B_{10}H_{10}$	127	12
300 keV Cryo $Na_2B_{10}H_{10}$	109	12
300 keV RT $Na_2B_{12}H_{12}$	49	6
300 keV Cryo $Na_2B_{12}H_{12}$	40	4

Table 3. SEM constant beam energy, current vs. time until sodium expulsion.

Change Current	**Cryogenic Temperature (s)**	**Room Temperature (s)**
5 keV 0.2 nA	1503	1133
5 keV 0.4 nA	792	607
5 keV 0.8 nA	252	312
5 keV 1.6 nA	141	172.3
5 keV 3.2 nA	88.3	99
5 keV 6.4 nA	50.5	53
5 keV 13 nA	23	30.3
5 keV 26 nA	5	8.7

Table 4. SEM constant current, beam energy vs. time until sodium expulsion.

Change Energy	**Cryogenic Temperature (s)**	**Room Temperature (s)**
1 keV 1.6 nA	204	120
2 keV 1.6 nA	65.5	14.7
5 keV 1.6 nA	127	172.3
10 keV 1.6 nA	300	535

References

Bai, S.; Liu, Z.; Cheng, D.; Lu, B.; Zaluzec, N. J.; Raghavendran, G.; Wang, S.; Marchese, T. S.; van Leer, B.; Li, L.; Jiang, L.; Stokes, A.; Cline, J. P.; Osmundsen, R.; Chen, M.; Barends, P.; Bright, A.; Zhang, M.; Meng, Y. S. (2026). Guidelines for Correlative Imaging and Analysis of Reactive Alkali Metal Battery Materials. *Joule*, 102311. https://doi.org/10.1016/j.joule.2025.102311.

Baker, L. A.; Rubinstein, J. L. (2010). Radiation Damage in Electron Cryomicroscopy. *Methods in Enzymology*; Jensen, G. J., (Eds.); Vol. 481, pp 371–388. Academic Press, https://doi.org/10.1016/S0076-6879(10)81015-8.

Banerjee, A.; Wang, X.; Fang, C.; Wu, E. A.; Meng, Y. S. (2020). Interfaces and Interphases in All-Solid-State Batteries with Inorganic Solid Electrolytes. *Chem Rev*. *120*, 6878. https://doi.org/10.1021/acs.chemrev.0c00101

Bradley, C. R. (1988). *Calculations of Atomic Sputtering and Displacement Cross-Sections in Solid Elements by Electrons with Energies from Threshold to 1.5 MeV*; ANL Technical Report; 88–48, https://doi.org/10.2172/6493690.

Bradley, C. R.; Zaluzec, N. J. (1989). Atomic Sputtering in the Analytical Electron Microscope. *Ultramicroscopy*, *28* (1), 335–338. https://doi.org/10.1016/0304-3991(89)90320-3.

Boebinger, M. G., Lewis, J. A., Sandoval, S. E. & McDowell, M. T. (2020). Understanding Transformations in Battery Materials Using in Situ and Operando Experiments: Progress and Outlook. ACS Energy Lett. 5, 335-345 https://doi.org/10.1021/acsenergylett.9b02514.

Cazaux, J. (1993). Some Physical Descriptions of the Charging Effects in Insulators Under Irradiation. In *Ionization of Solids by Heavy Particles*; Baragiola, R. A., (Ed.); Springer US: Boston, MA, pp 325–350. https://doi.org/10.1007/978-1-4615-2840-1_23.

Cazaux, J. (1995). Correlations between Ionization Radiation Damage and Charging Effects in Transmission Electron Microscopy. *Ultramicroscopy*, *60* (3), 411–425. https://doi.org/10.1016/0304-3991(95)00077-1.

Cazaux, J. (1999). Some Considerations on the Secondary Electron Emission, δ, from E− Irradiated Insulators. *J. Appl. Phys.*, *85* (2), 1137–1147. https://doi.org/10.1063/1.369239.

Cazaux, J. (2004). Charging in Scanning Electron Microscopy “from inside and Outside.” *Scanning*, *26* (4), 181–203. https://doi.org/10.1002/sca.4950260406.

Cazaux, J. (2006). E-Induced Secondary Electron Emission Yield of Insulators and Charging Effects. *Nucl. Instrum. Methods Phys. Res. Sect. B Beam Interact. Mater. At.*, *244* (2), 307–322. https://doi.org/10.1016/j.nimb.2005.10.006.

Cheng, D., Lu, B., Raghavendran, G., Zhang, M. & Meng, Y. S. (2020). Leveraging cryogenic electron microscopy for advancing battery design. Matter. 5, 26-42. https://doi.org/10.1016/j.matt.2021.11.019.

Comet, M., Dijkman, P. M., Boer Iwema, R., Franke, T., Masiulis, S., Schampers, R., Raschdorf, O., Grollios, F., Pryor, E. E., Jr., & Drulyte, I. (2024). Tomo Live: an on-the-fly reconstruction

pipeline to judge data quality for cryo-electron tomography workflows. *Acta Crystallographica Section D: Structural Biology*, 80(4), 247–258. https://doi.org/10.1107/S2059798324001840.

Deysher, G.; Chen, Y.-T.; Sayahpour, B.; Lin, S. W.-H.; Ham, S.-Y.; Ridley, P.; Cronk, A.; Wu, E. A.; Tan, D. H. S.; Doux, J.-M.; Oh, J. A. S.; Jang, J.; Nguyen, L. H. B.; Meng, Y. S. (2022). Evaluating Electrolyte–Anode Interface Stability in Sodium All-Solid-State Batteries. *ACS Appl. Mater. Interfaces*, *14* (42), 47706–47715. https://doi.org/10.1021/acsami.2c12759.

Deysher, G.; Oh, J. A. S.; Chen, Y.-T.; Sayahpour, B.; Ham, S.-Y.; Cheng, D.; Ridley, P.; Cronk, A.; Lin, S. W.-H.; Qian, K.; Nguyen, L. H. B.; Jang, J.; Meng, Y. S. (2024). Design Principles for Enabling an Anode-Free Sodium All-Solid-State Battery. *Nat. Energy*. *9* (9), 1161–1172. https://doi.org/10.1038/s41560-024-01569-9.

Demers, H., Poirier-Demers, N., Couture, A. R., Joly, D., Guilmain, M., de Jonge, N., & Drouin, D. (2011). Three-dimensional electron microscopy simulation with the CASINO Monte Carlo software. *Scanning*, 33(3), 135–146. https://doi.org/10.1002/sca.20262

Duchêne, L.; Kühnel, R.-S.; Rentsch, D.; Remhof, A.; Hagemann, H.; Battaglia, C. (2017). A Highly Stable Sodium Solid-State Electrolyte Based on a Dodeca/Deca-Borate Equimolar Mixture. *Chem Commun*, *53*, 4195. https://doi.org/10.1039/C7CC00794A.

Duchêne, L.; Lunghammer, S.; Burankova, T.; Liao, W.-C.; Embs, J. P.; Copéret, C.; Wilkening, H. M. R.; Remhof, A.; Hagemann, H.; Battaglia, C. (2019). Ionic Conduction Mechanism in the Na2(B12H12)0.5(B10H10)0.5 Closo-Borate Solid-State Electrolyte: Interplay of Disorder and Ion–Ion Interactions. *Chem. Mater. 31* (9), 3449–3460. https://doi.org/10.1021/acs.chemmater.9b00610.

Egerton, R. F.; Li, P.; Malac, M. (2004). Radiation Damage in the TEM and SEM. *Int. Wuhan Symp. Adv. Electron Microsc*, *35* (6), 399–409. https://doi.org/10.1016/j.micron.2004.02.003.

Egerton, R. F. (2014). Choice of Operating Voltage for a Transmission Electron Microscope. *Low-Volt. Electron Microsc.*, *145*, 85–93. https://doi.org/10.1016/j.ultramic.2013.10.019.

Han, B.; Li, X.; Bai, S.; Zou, Y.; Lu, B.; Zhang, M.; Ma, X.; Chang, Z.; Meng, Y. S.; Gu, M. (2021). Conformal Three-Dimensional Interphase of Li Metal Anode Revealed by Low-Dose Cryoelectron Microscopy. *Matter*, *4* (11), 3741–3752. https://doi.org/10.1016/j.matt.2021.09.019.

Heyd, J.; Scuseria, G. E.; Ernzerhof, M. (2003). Hybrid Functionals Based on a Screened Coulomb Potential. J. Chem. Phys., 118 (18), 8207–8215. https://doi.org/10.1063/1.1564060.

Jiang, N.; Su, D.; Spence, J. C. H. (2007). Sodium Reconstruction on Surface of Silicate Glasses in Transmission Electron Microscope. *Appl. Phys. Lett.*, *91* (23), 231906. https://doi.org/10.1063/1.2822402.

Jiang, N. (2008). Beam Damage by the Induced Electric Field in Transmission Electron Microscopy. *Micron*, *83*, 79–92. https://doi.org/10.1016/j.micron.2016.02.007.

Jiang, N. (2012). On the Limitation of Quantitative Measurements Using Transmission Electron Microscopy. *J. Non-Cryst. Solids*, *358* (1), 119–123. https://doi.org/10.1016/j.jnoncrysol.2011.09.004.

Jiang, N. (2015). Electron Beam Damage in Oxides: A Review. *Rep. Prog. Phys.*, *79* (1), https://doi.org/10.1088/0034-4885/79/1/016501

Jin, M.; Xu, D.; Su, Z.; He, Z.; Chen, X.; Wu, R.; Guo, Y. (2024). A Practical Nonflammable Na4B36H34-Based Hydroborate Electrolyte for High-Voltage All-Solid-State Sodium Batteries. *ACS Energy Lett.* , *9* (3), 1176–1183. https://doi.org/10.1021/acsenergylett.4c00112.

K Kanaya; S Okayama. (1972). Penetration and Energy-Loss Theory of Electrons in Solid Targets. *J. Phys. Appl. Phys.*, *5* (1), 43. https://doi.org/10.1088/0022-3727/5/1/308.

Li, X.; Han, B.; Yang, X.; Deng, Z.; Zou, Y.; Shi, X.; Wang, L.; Zhao, Y.; Wu, S.; Gu, M. (2021). Three-Dimensional Visualization of Lithium Metal Anode via Low-Dose Cryogenic Electron Microscopy Tomography. *iScience*, *24* (12). https://doi.org/10.1016/j.isci.2021.103418.

Liang, C.; Zhang, X.; Xia, S.; Wang, Z.; Wu, J.; Yuan, B.; Luo, X.; Liu, W.; Liu, W.; Yu, Y. (2020). Unravelling the Room-Temperature Atomic Structure and Growth Kinetics of Lithium Metal. *Nat. Commun.*, *11* (1), 5367. https://doi.org/10.1038/s41467-020-19206-w.

Lin, Y.; Joy, D. C. (2005). A New Examination of Secondary Electron Yield Data. *Surf. Interface Anal.*, *37* (11), 895–900. https://doi.org/10.1002/sia.2107.

Malis, T.; Cheng, S. C.; Egerton, R. F. (1988). EELS Log-Ratio Technique for Specimen-Thickness Measurement in the TEM. *J. Electron Microsc. Tech.*, *8* (2), 193–200. https://doi.org/10.1002/jemt.1060080206.

Paetzold, P.; Bettinger, H. F.; Volkov, O. (2007). The Anions [B24H23]3− and [B36H34]4− from the Thermal Protolysis of [B12H12]2−. *Z. Für Anorg. Allg. Chem.*, *633* (5–6), 846–850. https://doi.org/10.1002/zaac.200700001.

Peng, X.; Tu, Q.; Zhang, Y.; Jun, K.; Shen, F.; Ogunfunmi, T.; Sun, Y.; Tucker, M. C.; Ceder, G.; Scott, M. C. (2023). Unraveling Li Growth Kinetics in Solid Electrolytes Due to Electron Beam Charging. *Sci. Adv. 9* (17), eabq3285. https://doi.org/10.1126/sciadv.abq3285.

Seiler, H. (1983). Secondary Electron Emission in the Scanning Electron Microscope. *J. Appl. Phys*, *54* (11), R1–R18. https://doi.org/10.1063/1.332840.

Tanuma, S.; Powell, C. J.; Penn, D. R. (1994). Calculations of Electron Inelastic Mean Free Paths. V. Data for 14 Organic Compounds over the 50–2000 eV Range. *Surf. Interface Anal.*, *21* (3), 165–176. https://doi.org/10.1002/sia.740210302.

Wang, X.; Zhang, M.; Alvarado, J.; Wang, S.; Sina, M.; Lu, B.; Bouwer, J.; Xu, W.; Xiao, J.; Zhang, J.-G.; Liu, J.; Meng, Y. S. (2017). New Insights on the Structure of Electrochemically Deposited Lithium Metal and Its Solid Electrolyte Interphases via Cryogenic TEM. *Nano Lett.* *17* (12), 7606–7612. https://doi.org/10.1021/acs.nanolett.7b03606.

Yoshida, K.; Sato, T.; Unemoto, A.; Matsuo, M.; Ikeshoji, T.; Udovic, T. J.; Orimo, S. (2017). Fast Sodium Ionic Conduction in Na2B10H10-Na2B12H12 Pseudo-Binary Complex Hydride and Application to a Bulk-Type All-Solid-State Battery. *Appl Phys Lett*. *110*, 103901. https://doi.org/10.1063/1.4977885.

Zachman, M. J., Tu, Z., Choudhury, S., Archer, L. A. & Kourkoutis, L. F. (2018). Cryo-STEM Mapping of Solid–Liquid Interfaces and Dendrites in Lithium-Metal Batteries. Nature. 560 (7718), 345-349. https://doi.org/10.1038/s41586-018-0397-3.

Zaluzec, N. J. (2019). Temporally Resolved HyperSpectral Analysis vs Radiation Damage in Hard and Soft Matter. *Microsc. Microanal.*, *25* (S2), 1634–1635. https://doi.org/10.1017/S1431927619008900.

Zaluzec, N. J. (2021). First Light on the Argonne PicoProbe and The X-Ray Perimeter Array Detector (XPAD). *Microsc. Microanal.*, *27* (S1), 2070–2074. https://doi.org/10.1017/S1431927621007492.

Zemek, J.; Houdkova, J.; Jiricek, P.; Jablonski, A.; Jurka, V.; Kub, J. (2009). Determination of Electron Inelastic Mean Free Paths for Poly[Methyl(Phenyl)Silylene] Films. *Polymer*, *50* (11), 2445–2450. https://doi.org/10.1016/j.polymer.2009.03.031.